

Astronomy & Astrophysics manuscript no.
(will be inserted by hand later)

B1422+231: The influence of mass substructure on strong lensing

M. Bradač¹, P. Schneider¹, M. Steinmetz², M. Lombardi¹, L. J. King^{1,3}, and R. Porcas⁴

¹ Institut für Astrophysik und Extraterrestrische Forschung, Auf dem Hügel 71, D-53121 Bonn, Germany

² Steward Observatory, 933 North Cherry Avenue, Tucson, AZ 85721, USA

³ Max Planck Institut für Astrophysik, Karl-Schwarzschild Str. 1, D-85748 Garching bei München, Germany

⁴ Max-Planck-Institut für Radioastronomie, Auf dem Hügel 69, D-53121 Bonn, Germany

Submitted to A&A, December 3, 2001

Abstract. In this work we investigate the gravitationally lensed system B1422+231. High-quality VLBI image positions, fluxes and shapes as well as an optical HST lens galaxy position are used. First, two simple and smooth models for the lens galaxy are applied to fit observed image positions and fluxes; no even remotely acceptable model was found. Then, models with more complexity are considered, still not giving satisfactory results. Such models also do not accurately reproduce the image shapes. In order to fit the data successfully, mass substructure has to be added to the lens, and its level is estimated. To explore expectations about the level of substructure in galaxies and its influence on strong lensing, N-body simulation results of a model galaxy are employed. By using the mass distribution of this model galaxy as a lens, synthetic data sets of different four image system configurations are generated and simple lens models are again applied to fit them. The difficulties in fitting these lens systems turn out to be similar to the case of some real gravitationally lensed systems, thus possibly providing evidence for the presence and strong influence of substructure in the primary lens galaxy.

Key words. cosmology: dark matter – galaxies: substructure – gravitational lensing

1. Introduction

Gravitational lens systems with multiply imaged quasars are an excellent tool for studying the properties of distant galaxies. In particular, they provide the most accurate mass measures for the lensing galaxy. Besides the mass profiles, one can also gain information about evolution (Kochanek et al. 2000) and extinction laws (Fassnacht et al. 1999). Strong lensing is also a very promising and robust tool to measure the Hubble constant (Refsdal 1964). The success of this method, however, depends strongly on how well the mass model is constrained.

It turns out that image positions can be fit quite accurately with simple, smooth elliptical models (Keeton et al. 1997). Since the number of observational constraints from image positions is small, one wants to include the flux information. The optical fluxes, however, should not be used, as they might be affected by microlensing and/or dust obscuration (Chang & Refsdal 1979). Radio fluxes, on the other hand, can provide further constraints in lens modelling.

Fitting the fluxes very accurately turns out to be difficult in many lens systems. Models for MG0414+0534 (Falco et al. 1997; Keeton et al. 1997), PG1115+080 (Keeton & Kochanek 1997) and B1422+231 (e.g. Kormann et al. 1994) all show the same failure, namely the observed flux ratios are very different from what one would expect for the image configurations from a smooth model. In particular, the gravitational lens system B1422+231 was explored in detail, and as was first mentioned by Mao & Schneider (1998), mass substructure in the lens galaxy might provide an explanation for the failures in flux modelling. In recent works (Metcalf & Madau 2001; Chiba 2001) the effects of substructure in lens systems was further investigated.

A question arises as to whether there is something special about these quadruple systems, or does the discrepancy simply arise due to the fact that our smooth models are oversimplified? In other words, we are asking how “well” (for the purpose of strong lensing) can the smooth models used to fit the data represent a real galaxy? N-body simulation data can provide a realistic description of a galaxy mass distribution, thus giving a possibility to probe its effect on strong lensing.

In this paper, we will study the influence of the substructure on the lens system B1422+231, using VLBI radio measurements of the system by Patnaik et al. (1999). In Sec. 2 we give a description of the lens system and data used. The method is outlined in Sect. 3 and the results on fitting the system with smooth mass model are presented. In Sect. 4 the model accounting for the substructure is presented and in Sect. 5 the deconvolved image shape information is added to the fit. Sect. 6 gives the description of the method used to investigate lensing by an N-body simulated galaxy. We describe how we obtained synthetic data of four image systems, and the results of fitting such systems with lens models are presented. Finally we draw some conclusions in Sect. 7.

This work is an abbreviated version of Bradač (2001). In the course of writing this paper, several related papers on substructure of lens galaxies have been submitted (Metcalf & Madau 2001; Chiba 2001; Dalal & Kochanek 2001; Metcalf & Zhao 2001).

2. The mystery of B1422+231

The gravitational lens system B1422+231 was discovered in the course of the JVAS survey (Jordell Bank – VLA Astrometric Survey) by Patnaik et al. (1992). It consists of four image components. The three brightest images A, B, and C (as designated by Patnaik et al. 1992) are fairly collinear. The radio flux ratio between images A and B is approximately 0.9, while image C is fainter (flux ratio C to B is approximately 0.5). Image D is further away and is much fainter than the other images (with flux ratio D:B of 0.03). The most recent available radio data for the image positions and fluxes were obtained from the polarisation observations made at 8.4 GHz using the VLBA and the 100m telescope at Effelsberg from Patnaik et al. (1999) and are listed in Table 1. For each of the components, the authors measured positions (relative to the image B) and fluxes as well as the deconvolved image shapes. Here and through the paper we are using a notation where (θ_1, θ_2) are the angular coordinates in the lens plane and (β_1, β_2) in the source plane. θ_1 and β_1 increase in the negative RA direction.

The radio source of this lens system is associated with a 15.5 mag quasar at a redshift of 3.62 (Patnaik et al. 1992). The lensing galaxy has been observed in the optical; its redshift has been determined to be 0.338 and its position relative to image B has been measured (Impey et al. 1996). The main lens galaxy is a member of a compact group with a median projected radius of $35 h^{-1}$ kpc and velocity dispersion of $\sim 550 \text{ km s}^{-1}$ (Kundic et al. 1997).

Several groups have tried to model B1422+231 (Hogg & Blandford 1994; Kormann et al. 1994; Keeton et al. 1997; Mao & Schneider 1998) and all of them have experienced difficulties in fitting it. As we used data with even more precise image positions one might expect that it would become even harder to model the system. However, as already pointed out by some authors, the difficulties do

not lie in fitting the image positions but rather in the flux ratios.

It turns out that simple, smooth models fail to reproduce the radio as well as the optical flux ratios of the system. While the mismatch in optical data might still be due to the microlensing and/or dust obscurations, this can probably not explain why such models are not successful when fitting radio flux ratios. Mao & Schneider (1998) have proposed a lens model that accounts for the substructure in the lensing galaxy. They concluded that one needs a surface mass density perturbation of the order of 1 % of the critical surface mass density in order to change the flux ratios to the observed values.

In order to succeed in fitting the image flux ratios, one needs to consider more sophisticated models. However, such models also require the use of additional parameters. Therefore it is very difficult to ensure a constrained model that accounts for the substructure using as constraints only image positions, flux ratios, and the galaxy position. For this reason we also included the axis ratios and the orientation angles of the deconvolved images as additional constraints. They were obtained from Patnaik et al. (1999) and are given in Table 2. Listed are the absolute values of ellipticities and the orientation angles of the fitted elliptical Gaussians together with uncertainties.

From the configuration and fluxes of the four images we can gain some qualitative constraints on the lens model. Image D is much fainter than the rest which can mean that it is either highly demagnified or that the other three images are highly magnified. Because the position of the primary lens galaxy is known, the possibility of image D being highly demagnified is ruled out. Namely, image D does not lie at a position of high surface mass density and thus high demagnification. Images A, B, and C are therefore highly magnified. In order to get three highly magnified images with a fairly collinear configuration, the source has to lie close to (and inside) a cusp.

Table 1. Image positions with respect to image B and radio fluxes taken from Patnaik et al. (1999), where the uncertainties of the image positions were estimated to be 1/20th of the image size in the corresponding direction (note that these directions do not coincide with θ_1 and θ_2 directions). For simplicity we set the errors to be the same in both directions and assign the value of 0.05 mas for all images. $F^{i,\text{obs}}$ is the total radio flux density. The position of the galaxy (designated by G, measured in the optical) was taken from Impey et al. (1996).

Image	$\Delta\theta_1$ in mas	$\Delta\theta_2$ in mas	$\sigma_{\text{RA, Dec}}$ in mas	$F^{i,\text{obs}}$ mJy	$\sigma_{i,\text{flux}}$ mJy
A	-389.25	319.98	0.05	152	2
B	0.0	0.0		164	2
C	333.88	-747.71	0.05	81	1
D	-950.65	-802.15	0.05	5	0.5
G	-717	-640		8	

For a source position sufficiently close to and inside a cusp there exists a relation which states that the sum of the fluxes of the outer two magnified images (in our case images A and C) is the same as the flux of the middle image – B (Schneider & Weiss 1992). This rule is strongly violated in the lens system B1422+231. Actually, one can get a deviation from this relation if the source is away from the cusp or if there is substructure in the system (i.e. fluctuations on a scale smaller than the separations between A, B, and C). The elongations of the images indicate that the source is indeed close to a cusp and thus argue in favour of substructure in the system.

3. Lens modelling

First we considered two standard gravitational lens models since their application to the Patnaik et al. (1999) data has not yet been discussed in the literature.

The standard approach to model a strong lens system is to define the goodness-of-fit function χ^2 , a measure of the deviation of the predicted and observed image properties. We perform the minimisation in the image plane. The χ^2 for the positions of the images reads

$$\chi_{\text{pos}}^2 = \sum_{i=1,3,4} \frac{|\Delta\theta^{i,\text{obs}} - \Delta\theta^{i,\text{mod}}|^2}{\sigma_{i,\text{pos}}^2}, \quad (1)$$

where $\Delta\theta^{i,\text{obs}}$ and $\Delta\theta^{i,\text{mod}}$ are the observed and the modelled position of the i -th image relative to a chosen origin (in our case image B, denoted by $i = 2$), respectively. Note that the sum extends only over the images A, C, and D.

Table 2. The absolute ellipticity $|\epsilon_i|$ – defined in Eq. (7) – and the position angle φ_i (measured w.r.t. the θ_1 -axis) of the deconvolved image i of the fitted elliptical Gaussians calculated from Patnaik et al. (1999) data. The uncertainty of the absolute ellipticity $\sigma_{|\epsilon|,i}$ is determined by taking the uncertainty on the major and minor axis to be a tenth of the beam size, which corresponds to 0.1 mas and we considered them to be uncorrelated

Image	$ \epsilon_i $	φ_i	$\sigma_{ \epsilon ,i}$	$\sigma_{\varphi,i}$
A	0.70	143°	0.07	5°
B	0.80	133°	0.07	5°
C	0.55	106°	0.09	5°
D	0.20	33°	0.10	20°

Table 3. The summary of parameters used for the lens galaxy mass models.

Model	Par.	Description
SIE+SH	θ_{lens}	lens position
	σ_v	Line-of-sight velocity dispersion
	ϵ	Absolute ellipticity
	ϕ	Position angle of ellipticity
	$\gamma_1^{\text{ext}}, \gamma_2^{\text{ext}}$	External shear components
NIE+SH	θ_c	Add. to SIE+SH, core radius

To be more precise, $\Delta\theta^{i,\text{mod}}$ is obtained as

$$\Delta\theta^{i,\text{mod}} = \theta^{i,\text{mod}} - \theta^{2,\text{mod}},$$

where the vectors $\theta^{i,\text{mod}}$ and $\theta^{2,\text{mod}}$ are measured with respect to an independent reference point. The same is true for $\Delta\theta^{i,\text{obs}}$,

$$\Delta\theta^{i,\text{obs}} = \theta^{i,\text{obs}} - \theta^{2,\text{obs}},$$

which is the observed image position as listed in Table 2. Therefore when the image positions of A, C, and D w.r.t. the image B are measured, they all contain the uncertainty of the origin (image B). Thus, the uncertainties of the measurements of each of the image positions are correlated and we are forced to calculate the χ_{pos}^2 as in (1). We therefore denote $\sigma_{i,\text{pos}}$ to be the uncertainty of the measured relative image position.

Similarly, we define for the galaxy position

$$\chi_{\text{galaxy}}^2 = \frac{|\Delta\theta_{\text{lens}}^{\text{obs}} - \Delta\theta_{\text{lens}}^{\text{mod}}|^2}{\sigma_{\text{gal, pos}}^2}, \quad (2)$$

with $\sigma_{\text{gal, pos}}$ being the uncertainty of the relative lens position. Here, additional problems might appear if the origin for positions in optical and radio do not necessarily coincide (i.e. the position of the galaxy is measured w.r.t. the optical position of image B, which might not necessarily be the same as the radio one). We assume this not to be the case in the limit of errors. The contribution to the χ^2 -function from the fluxes is given by

$$\chi_{\text{flux}}^2 = \sum_{i=1}^4 \frac{(F^{i,\text{obs}} - F^{i,\text{mod}})^2}{\sigma_{i,\text{flux}}^2}, \quad (3)$$

where $F^{i,\text{mod}}$ denotes the flux of the i -th image obtained from the model and $F^{i,\text{obs}}$ is the observed flux. The χ^2 function we want to minimise is simply given by the sum

$$\chi_{\text{tot}}^2 = \chi_{\text{pos}}^2 + \chi_{\text{galaxy}}^2 + \chi_{\text{flux}}^2. \quad (4)$$

In order to obtain the values of $\Delta\theta^{i,\text{mod}}$ from the lens equation (see e.g. Schneider et al. 1992), we used the Numerical Recipes MNEWT routine from Press et al. (1992) for solving a set of two non-linear equations. The χ^2 -function was then minimised with respect to the model parameters using POWELL, a multi-dimensional minimisation routine, also from Press et al. (1992).

3.1. Modelling B1422+231 with smooth models

We used a singular isothermal ellipsoid with external shear from Kormann et al. (1994) (hereafter SIE+SH) and a non-singular isothermal ellipsoid model with external shear (NIE+SH) from Keeton & Kochanek (1998) to fit the image positions and fluxes of B1422+231. The explanation of the model parameters for the models we used are given in Table 3.

We have applied the fitting procedure described above to the radio data, using image positions, fluxes, and their

uncertainties from Patnaik et al. (1999), listed in Table 1. The optical position of the galaxy was taken from Impey et al. (1996). Although the image positions are very accurate (of the order of 50 μ arcsec), we have no difficulties fitting them, and so the χ^2 contribution from the image positions drops to zero (see Table 4). However, as already pointed out in previous works on B1422+231, the model completely fails in predicting the image fluxes. In particular image A is predicted too dim (the modelled flux ratio A:B turned out to be 0.80, much below the measured value of 0.93).

We have also tried to model the system with a NIE+SH model; however, the χ^2 did not improve significantly.

4. Models with substructure

In the previous section it turned out that A:B flux ratio causes the biggest difficulty in fitting the B1422+231. Since the radio and optical flux ratios are very different, one is tempted to exclude it from the χ^2 measure (see Mao & Schneider 1998, Chiba 2001).

However, one can also try to deal with this problem in another way. Adding a small perturber at the same angular diameter distance as the primary lens and at approximately the same position as image A can change the flux ratio A:B substantially. On the other hand, calculations show, that such a perturber does not affect the positions of any of the images or the flux ratios of the other two images much.

We model the perturber as a non-singular isothermal sphere. This gives two additional parameters (two perturber positions, since we keep the line-of-sight velocity dispersion and core radius of the perturber fixed) to the macro (SIE+SH) model. The choice of the perturber being modelled as non-singular is due to the fact that a singular isothermal sphere (with the same Einstein radius) is more likely to give rise to additional (observable) images.

The number of degrees of freedom we have with such a model is 0. Using SIE+SH as a macro model and adding an additional perturber we have in total 14 parameters (we count the position and the unlensed flux of the source as parameters). Having 12 constraints (3 relative image positions, 4 fluxes and a galaxy position) such a model is underconstrained. Therefore, if the SIE+SH+NIS family of models is a realistic representation of the lensing galaxy we expect χ^2 to vanish.

4.1. Modelling B1422+231 using the substructure model

For modelling B1422+231 we fixed the line-of-sight velocity dispersion of the NIS perturber to $\sigma_{\text{NIS}} = 10 \text{ km s}^{-1}$ (equivalent to an Einstein radius of approximately 2 mas) and its core radius to $\theta_c = 20 \text{ mas}$. A perturber with these properties does not affect the image positions significantly; on the other hand it can substantially change the magnification at the position of one of the images.

When fixing the core radius one has to be aware that not only an SIS, but also an NIS lens with small enough core radius might give additional images. Therefore, an NIS perturber should have a core radius much bigger than the Einstein radius, in order not to produce additional images. We have checked that indeed no additional observable images are predicted by the model.

For this purpose we define the function f on a grid of points $\boldsymbol{\theta}_j$

$$f = |\boldsymbol{\beta}(\boldsymbol{\theta}_j) - \boldsymbol{\beta}_s|^2, \quad (5)$$

where $\boldsymbol{\beta}(\boldsymbol{\theta}_j)$ is the calculated source position corresponding to the point $\boldsymbol{\theta}_j$. The position $\boldsymbol{\beta}_s$ is defined as the average position for the source predicted by the four observed image positions

$$\boldsymbol{\beta}_s = \frac{1}{4} \sum_{i=1}^4 \boldsymbol{\beta}(\boldsymbol{\theta}^{i, \text{obs}}). \quad (6)$$

The function f vanishes only around the positions where images are observed. In our case we indeed found only four such regions, and they correspond to the four observed images.

The resulting model has 12 parameters, which leaves us 0 degrees of freedom. The χ^2 has decreased by a factor of more than 20 compared with the SIE+SH model; however, since we have zero degrees of freedom we expect χ^2 to vanish if the model is realistic (and if the χ^2 technique is an adequate method). The family of models considered thus does not seem to be adequate for the description of the galaxy in B1422+231 lens system.

Surprisingly, however, we see that the flux ratio of images A:B is not the only problem when dealing with fluxes. Adding a small perturber close to image A allows us to adjust the modelled flux of A such, that it does not give any contribution to the χ^2 -function. Still the remaining image fluxes are not fit perfectly, leading to a possible conclusion that all images are affected by the mass substructure.

5. Using image shapes as constraints

In order to ensure that the macro model with an additional perturber is constrained, we include the deconvolved im-

Table 4. Result of modelling B1422+231 radio positions and flux data with (i) an SIE model with external shear and (ii) an SIE model with external shear and an additional perturbing NIS galaxy. θ_c and σ_{NIS} of the perturbing galaxy were fixed to the values $\theta_c = 20 \text{ mas}$ and $\sigma_{\text{NIS}} = 10 \text{ km/s}$. The parameters of the best fitting model are listed in Table 7.

Model	N_{dof}	$\chi^2_{\text{tot}} = \chi^2_{\text{pos,rel}} + \chi^2_{\text{gal,rel}} + \chi^2_{\text{flux}}$
(i)	2	129 = 0 + 18 + 111
(ii)	0	5.6 = 0.0 + 0.8 + 4.8

age shapes in the fit. We work in terms of the complex ellipticity,

$$\epsilon_i := |\epsilon_i| e^{2i\varphi_i}.$$

Each image is thus described by the absolute value of ellipticity $|\epsilon_i|$ and the corresponding position angle φ_i (measured w.r.t. θ_1 -axis). From the given data the absolute value of ellipticity is calculated as

$$|\epsilon_i| = \frac{a_i - b_i}{a_i + b_i}, \quad (7)$$

where a_i and b_i are major and minor semi axes of the fitted elliptical Gaussian. Two additional terms,

$$\chi^2_\epsilon = \sum_{i=1}^4 \frac{(|\epsilon_i^{\text{obs}}| - |\epsilon_i^{\text{mod}}|)^2}{\sigma_{|\epsilon|,i}^2}, \quad (8)$$

and

$$\chi^2_\varphi = \sum_{i=1}^4 \frac{(\varphi_i^{\text{obs}} - \varphi_i^{\text{mod}})^2}{\sigma_{\varphi,i}^2}. \quad (9)$$

have to be added to the χ^2 -function. For simplicity we assumed the errors on ellipticity and position angle to be uncorrelated.

In order to get the values for the ellipticity as predicted by a given model one can work in terms of relative magnification matrices. These describe how an infinitesimal vector associated with one of the images is mapped onto an infinitesimal vector of another image. For this method one chooses a reference image in order not to have to include the information about the source ellipticity. The ellipticity of the reference image is thus treated as if it would be measured with absolute accuracy. However, one can get different results depending on the choice of the reference.

Therefore we decided to include two additional model parameters, namely the absolute ellipticity of the source $|\epsilon_s|$ and its orientation angle φ_s . The magnification tensor of the i -th image relative to the unlensed source $[\mu^{(i)}]$ is given by the inverse of the Jacobian matrix

$$[\mu^{(i)}] = A^{-1}(\theta^{(i)}). \quad (10)$$

The ellipticity of the image can be calculated from the reduced shear g and the ellipticity of the source ϵ_s . The reduced shear $g(\theta^i)$ at the position θ^i of image i is given by

$$g(\theta^{(i)}) = \frac{1}{1 - \kappa(\theta^{(i)})} (\gamma_1(\theta^{(i)}) + i \gamma_2(\theta^{(i)})), \quad (11)$$

where $\kappa(\theta^{(i)})$ is the dimensionless surface mass density and $\gamma_1(\theta^{(i)})$ and $\gamma_2(\theta^{(i)})$ are the shear components. For brevity we skip the position dependence in the notation below. Finally, the image ellipticity can be written as (e.g. Bartelmann & Schneider 2001)

$$\epsilon_i = \begin{cases} \frac{g + \epsilon_s}{1 + g^* \epsilon_s} & \text{for } |g| \leq 1 \\ \frac{1 + g^* \epsilon_s}{g^* + \epsilon_s^*} & \text{for } |g| > 1 \end{cases}. \quad (12)$$

We also calculate the reduced shear needed in order to recover the image ellipticity of the i -th image. For this purpose we evaluate g^* from one of the equations and then plug the result into the same equation again. For $|g| \leq 1$ we get

$$g = \frac{\epsilon_i (1 - |\epsilon_s|^2) - \epsilon_s (1 - |\epsilon_i|^2)}{1 - |\epsilon_i|^2 |\epsilon_s|^2}, \quad (13)$$

and for $|g| > 1$ the calculation yields

$$g = \frac{\epsilon_i (1 - |\epsilon_s|^2) + \epsilon_s (1 - |\epsilon_i|^2)}{|\epsilon_i|^2 - |\epsilon_s|^2}. \quad (14)$$

5.1. Fitting deconvolved image shapes of B1422+231

In this section we use image positions, fluxes (see Table 1), and deconvolved image shapes (see Table 2) for to constrain SIE+SH+NIS model. The χ^2 minimisation was done according to the previous section, and the results are presented in Table 5. We have decreased the value of the core radius of the perturber in order to get higher magnification gradients and thus be able to change individual image properties even more. Again, no additional observable images are produced by the perturber(s).

In the Patnaik et al. (1999) paper the uncertainties on the image shapes are not listed. The image shapes are obtained by fitting Gaussian profiles to the map, and then deconvolved using the known beam-shape. The uncertainties are therefore just a rough estimate, since one can not quantitatively account for the error of such fitting. In fact, all the images exhibit non-Gaussian features a Gaussian model is an oversimplification for the image shape description.

The resulting χ^2 for the minimisation was 19, having 6 degrees of freedom (the probability of obtaining a value for χ^2 bigger than 19 is 0.0042). We further try to fit the data with two perturbers in the system. If we put two equal perturbers into the system (i.e. both with fixed $\theta_c = 1$ mas and $\sigma_{\text{NIS}} = 10$ km/s), we get a χ^2 of 15 (see Table 5) with 4 degrees of freedom. The probability of obtaining a χ^2 larger than that value is now 0.0047. Such a reduction of

Table 5. Result of modelling B1422+231 radio positions, flux and image shape data with the SIE model with external shear (iii), SIE+SH and *one* additional perturbing NIS galaxy (iv), and SIE+SH with *two* perturbing galaxies (v). The core radius and σ_{NIS} of the perturbing galaxy(ies) were fixed to the values $\theta_c = 1$ mas and $\sigma_{\text{NIS}} = 10$ km/s. The parameters of the best fitting models are listed in Table 7.

Model	N_{dof}	$\chi^2_{\text{tot}} = \chi^2_{\text{pos,rel}} + \chi^2_{\text{gal,rel}} + \chi^2_{\text{flux}} + \chi^2_\epsilon + \chi^2_\varphi$
(iii)	8	140 = 0 + 18 + 111 + 4 + 7
(iv)	6	19 = 0 + 0 + 6 + 9 + 4
(v)	4	15 = 0 + 0 + 4 + 7 + 4

χ^2 is apparently not a significant improvement of the fit (compared to the model with a single perturber).

Just for comparison, we also include the deconvolved image shapes in the fit with SIE+SH model. The resulting χ^2 is 140 for 8 degrees of freedom (the probability of obtaining a value for χ^2 larger than that is now only 10^{-28}). We essentially get the same model as when only fitting image positions and fluxes (see Table 7). We see that the fluxes provide much stronger constraints (their uncertainty is much smaller) than the image shapes.

Apparently, models with substructure yield significantly better fits than the ones without. However, we should stress that, strictly speaking, the appropriate statistical treatment can not be easily performed because the model parameters enter the χ^2 function in a non-linear way. As a result, the χ^2 function does *not* behave as a chi-square random variable with the appropriate number of degrees of freedom. One can see that already from the fact that the χ^2 function did not vanish when using a model with zero degrees of freedom. Hence, the probabilities we quoted above have to be taken with care; still they can be used to compare the performance of different models.

From Eqs. (13) and (14) we can determine the reduced shear g at the position of each of the images needed to recover the observed shapes of the images. Further we define an estimate \tilde{g}_i that gives a difference between the reduced shear g^{mod} of the best fit (smooth) SIE+SH model for the image positions and fluxes – i.e. model (ii) – and the reduced shear g needed in order to represent the observed image shapes for the i -th image;

$$\tilde{g}_i = g - g^{\text{mod}}.$$

The values for the images A, B, and C are

$$\tilde{g}_A = -0.2 + 0.0 i,$$

$$\tilde{g}_B = 0.1 - 0.1 i,$$

$$\tilde{g}_C = 0.2 - 0.1 i.$$

We have not included image D in the estimate, since the errors on measurements of its shape are very large. Furthermore, these estimates have to be treated with care, as the unlensed ellipticity of the source is unknown. The estimates also do not account for errors in observed image shapes.

In order to calculate the estimates given above we took the values for g^{mod} from the best fitting SIE+SH model (see Table 6) and for ϵ_s from the best fitting SIE+SH+NIS model that included ellipticities in the fit – see Table 5, model (iv). Note, however, that the estimates are not very sensitive to the value of ϵ_s .

It is clear that it is difficult to simultaneously stretch and rotate the images with one (or two) perturber(s). The macro-model is not very successful in predicting both components of the image ellipticities, and therefore corrections are needed in the case of all four images. At this stage, one can seriously ask oneself how accurately do the models considered above represent the strong lensing properties of a real galaxy.

6. Strong lensing by an N-body simulated galaxy

A question that arises from model fitting of B1422+231 is how “well” (for the purpose of strong lensing) the smooth models we used can represent a realistic galaxy. The most accurate description of the mass distribution in a realistic galaxy can be taken from N-body simulations. We used the cosmological N-body simulation data including gasdynamics and star formation of Steinmetz & Navarro (2001) for this purpose.

The simulations were performed using GRAPESPH, a code that combines the hardware N-body integrator GRAPE with the Smooth Particle Hydrodynamics technique (Steinmetz 1996). GRAPESPH is fully Lagrangian and optimally suited to study the formation of highly non-linear systems in a cosmological context. The version used here includes the self-gravity of gas, stars, and dark matter components, a three-dimensional treatment of the hydrodynamics of the gas, Compton and radiative cooling (assuming primordial abundances), the effects of a photoionizing UV background, and a simple recipe for transforming gas into stars.

The original simulated field is located at $z = 0.2$ and contains approximately 300000 particles. The simulation is contained within a sphere of diameter 32 Mpc which is split into a high resolution sphere of diameter 2.5 Mpc centred around a galaxy and an outer low resolution shell.

Table 6. Values for κ , γ_1 and γ_2 corresponding to the best fitting SIE+SH model given in Table 7.

Image	κ	γ_1	γ_2
A	0.38	0.25	-0.40
B	0.47	-0.10	-0.62
C	0.36	-0.40	-0.10
D	1.89	-0.71	-1.93

Table 7. Resulting parameters from best fitting models: (i) SIE+SH, (ii) SIE+SH+NIS, (iii) SIE+SH, (iv) SIE+SH+NIS, (v) SIE+SH+2NIS, where in models (iii), (iv) and (v) we use the shapes of the images as additional constraints. θ_{NIS} is the position of the perturber(s). The parameters of the best fitting source shape were $|\epsilon^s| = 0.14$ and $\varphi^s = 60^\circ$ for the model (iii), for the model (iv) $|\epsilon^s| = 0.04$, $\varphi^s = 30^\circ$, and for the model (v) $|\epsilon^s| = 0.10$, $\varphi^s = 20^\circ$. The position angles are measured w.r.t. θ_1 -axis. The resulting line-of-sight velocity dispersion σ_v was 190 km s $^{-1}$ in all four cases.

	θ_{lens} (mas, mas)	ϵ_{gal}	ϕ	γ_1^{ext}	γ_2^{ext}	θ_{NIS} (mas, mas)
(i)	(-744, -659)	0.19	34 $^\circ$	-0.04	-0.16	
(ii)	(-722, -646)	0.13	32 $^\circ$	-0.05	-0.18	(-348, 356)
(iii)	(-744, -659)	0.19	34 $^\circ$	-0.04	-0.16	
(iv)	(-718, -643)	0.12	32 $^\circ$	-0.05	-0.18	(-336, -367)
(v)	(-719, -641)	0.13	32 $^\circ$	-0.05	-0.18	(-407, 327) (-956, 806)

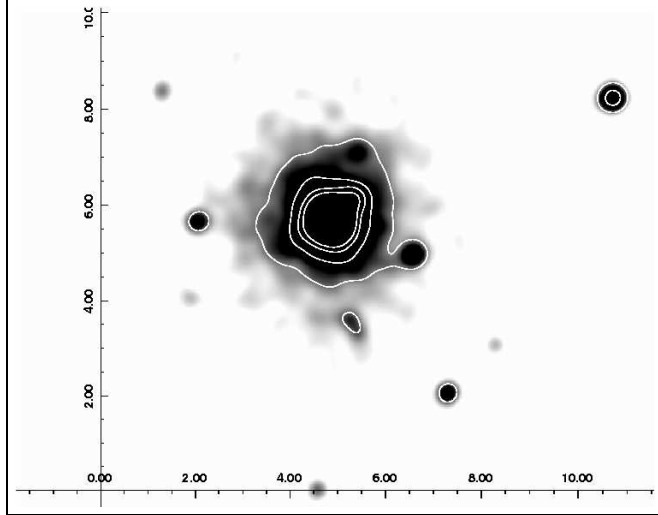


Fig. 1. The cut-out of the surface mass density map of the simulated galaxy. The mass distribution resulting from the cosmological N-body simulation (see text) was smoothed using convolution with a Gaussian kernel characterised by a standard deviation $\sigma \sim 0.8$ kpc ~ 0.2 arcsec. This map was then evaluated on 2048×2048 grid points ($\sim 160 \times 160$ kpc) and the surface mass density was calculated. Test particles, used in the N-body simulation to account for the large-scale structure, have been removed here. The contours correspond to the values of $\kappa = 0.8; 1.6; 2.4; 3.2$. The dark regions represent the regions of high κ . The units on the axes are arcseconds, one arcsecond in the *lens* plane corresponds to approximately 4 kpc.

Gas dynamics and star formation is restricted to the high resolution sphere (280000 particles, 92000 of which dark matter), while the 34000 dark matter particles of the low resolution sphere sample the large scale matter distribution in order to appropriately reproduce the large scale tidal fields (see Navarro & Steinmetz 1997 and Steinmetz & Navarro 2000 for details on this simulation technique).

The simulation was performed in a Λ CDM cosmology ($\Omega_0 = 0.3$, $\Omega_\Lambda = 0.7$, $\Omega_b = 0.019/h^2$, $\sigma_8 = 0.9$). It has a mass resolution of $1.26 \times 10^7 M_\odot$ and a spatial resolution of 0.5 kpc. A realistic resolution scale for an identified substructure is typically assumed to be ~ 40 particles which corresponds to $5 \times 10^8 M_\odot$. The quoted mass resolution holds for gas/stars. The high resolution dark matter particles are about a factor of 6 ($= \Omega_0/\Omega_b$) more massive.

From the original simulated field we took a cut-out map of size $\sim 160 \times 160$ kpc that is centred on a single galaxy. This area lies well within the high resolution sphere and is void of any massive intruder particles from the low resolution shell. The resulting mass distribution was smoothed using convolution with a Gaussian kernel characterised by a standard deviation of $\sigma \sim$

0.8 kpc ~ 0.2 arcsec.¹ This map was then evaluated on 2048×2048 grid points. The final map contains information about approximately 130000 particles with a total mass of $3.0 \times 10^{12} M_\odot$. The surface mass density κ was calculated for every grid point. We chose the redshift of the source to be $z = 3$. A part of the cut-out map can be seen in Fig. 1.

The lens properties are calculated on a grid of 2048×2048 points. The Poisson equation

$$\nabla^2 \psi(\boldsymbol{\theta}) = 2 \kappa(\boldsymbol{\theta}) . \quad (15)$$

is solved (on the grid) in Fourier space by the FFT (Fast Fourier Transformation) method. This method is incorporated in the routine KAPPA2STUFF from the IMCAT software of Nick Kaiser (<http://www.ifa.hawaii.edu/~kaiser>) that we used. It takes a grid map of $\kappa(\boldsymbol{\theta}_j)$ as an input and returns the values of deflection angle and complex shear (in \boldsymbol{x} -space), along with other quantities. From these data we calculated the Jacobi matrix for each grid point.

The simulated galaxy is a field galaxy. Therefore we add two external shear components to the Jacobi matrix (evaluated at each grid point) in order to make it similar to the galaxy in B1422+231. The shear components were taken to be the same as the ones obtained from the best fitting SIE+SH model

$$\gamma_1^{\text{ext}} = -0.04, \quad \gamma_2^{\text{ext}} = -0.16 .$$

The external shear accounts for the effect of the neighbouring galaxies of the compact group, which are not present in the simulation.

Fig. 2 shows the magnification map of the surface mass density (given in Fig. 1) with additional external shear. One can clearly see the outer critical curve (white curve), while only the traces of the inner critical curve are visible (little circle inside the black region). The reason why we can see the outer critical curve so much better than the inner one is the following. At the centre $\boldsymbol{\theta}_c$ of the galaxy, the surface mass density is very high and the determinant of the Jacobi matrix can be approximated by $\det A \sim \kappa(\boldsymbol{\theta}_c)^2$. In our particular case, $\kappa(\boldsymbol{\theta}_c) \approx 50$, and since at the critical curve $\det A = 0$, we see that the determinant has to decrease from 2500 to 0 in a region of 0.4 arcsec. The transition is therefore very steep and we have a very good chance to miss the maximum value of magnification there, since the resolution is not high enough. At the outer critical curve, the change is slower and we can clearly see the points of high magnification.

In order to generate a similar image configuration as the one in B1422+231, one considers the caustic curve. This can be done by simply mapping the points of high magnification onto the source plane. Such a map is presented in Fig. 3.

¹ For the calculations through the paper we assumed an Einstein-de-Sitter Universe and the Hubble constant $H_0 = 65 \text{ km s}^{-1} \text{ Mpc}^{-1}$.

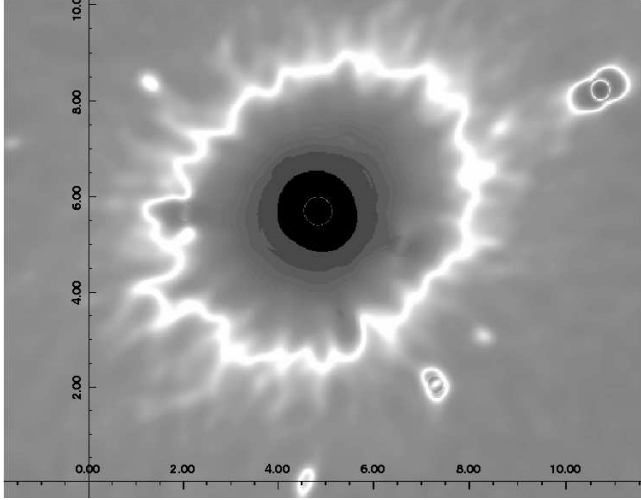


Fig. 2. The magnification map of the simulated galaxy calculated using the KAPPASTUFF routine from Nick Kaiser's software IMCAT. External shear is added in the evaluation of the magnification map for to account for neighbouring galaxies (see text). Lighter regions represent high magnifications. The units on the axes are arcseconds, one arcsecond in the *lens* plane corresponds to approximately 4 kpc.

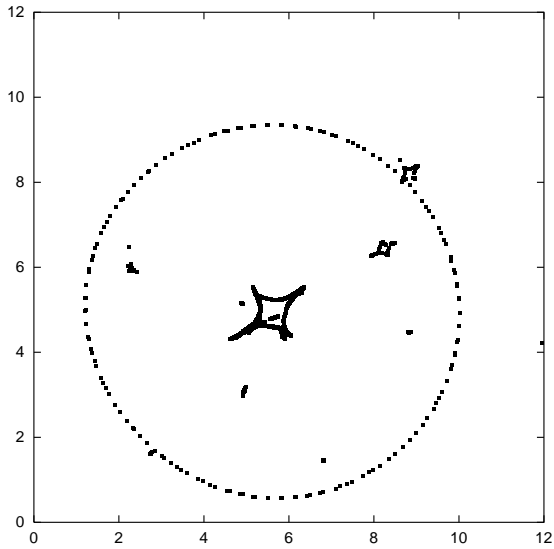


Fig. 3. The caustic obtained by mapping the points of high magnification onto the source plane. We took $|\mu| > 100$ for the inner caustic, for the outer one we additionally picked the points of $|\mu| > 0.5$ from the central part of the magnification map. The units on the axes are arcseconds, one arcsecond in the *source* plane corresponds to approximately 6 kpc for the source at $z = 3$.

On first sight the caustic structure of the N-body simulated galaxy looks the same as e.g. the caustic of the smooth NIE model with a small core radius. However, if we look only at the inner, asteroid caustic we can see that it is not completely “smooth”. With the help of bilinear

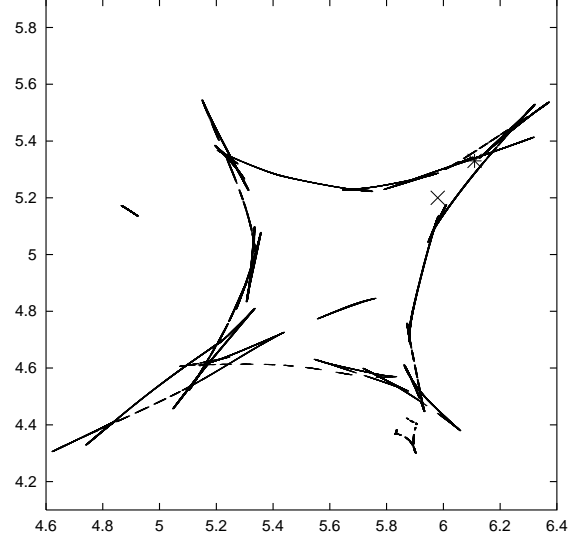


Fig. 4. The caustic curves obtained by first interpolating the magnification map on a refined grid using bilinear interpolation (increasing the number of points in the region of interest by a factor of 25) and mapping the points of high magnification $|\mu| > 100$ (Fig. 2) to the source plane. The units on the axes are arcseconds, one arcsecond in the *source* plane corresponds to approximately 6 kpc for the source at $z = 3$. Two marks correspond to the source position of data set 1 (cross) and 11 (star) – see Sect. 6.1. The source positions of other data sets are located on a line connecting them.

interpolation we recalculated the magnification map on a refined grid (increasing the number of points being evaluated by 5×5) and the corresponding caustic for such a grid is shown in Fig. 4. The caustic structure is much more complicated than in the case of a smooth model; in addition to folds and cusps we also have swallowtails formed (see Schneider et al. 1992 for more details on catastrophe theory).

6.1. Generating synthetic data

We select a source position β_s such as to lie inside the asteroid caustic and close to the cusp, trying to chose a position for which we would get similar flux ratios as in the case of B1422+231. In total we considered 11 different source positions (see Fig. 4).

For each of them we first determine approximate image positions using the method described in Sect. 4.1. In order to get exact image positions we use the root finding method MNEWT again, for which we need the deflection angle to be continuous inside the region where we look for images. In our case the deflection angle is defined only on a 2048×2048 grid. We perform bilinear interpolation between grid points. Having the image positions, we performed bilinear interpolation of the magnification map in order to get more exact magnification factors.

6.2. Fitting the synthetic data

For the χ^2 -fitting method according to (4) we need to determine the uncertainty on the image positions and fluxes. Since we use interpolation for the MNEWT method we do not have a real estimate for the errors. One can, for example, set the errors to the same (relative) values as the uncertainties on the observed radio positions in B1422+231. For the typical scales we are using here (i.e. the distance B to D is approximately 3.5 arcsec) this would mean an uncertainty of much less than a distance between two grid points. However, such a small error estimate is not realistic; due to the finite grid we estimate the image position uncertainties to be the distance between two grid points (which is a generous estimate; we use bilinear interpolation so the uncertainty is probably lower). The flux ratio errors were then set to be approximately 2 % for images A, B and C and 5 % for image D. These uncertainties are set to be the same as in the case of observed radio fluxes in B1422+231. The galaxy position error is set twice as big as that for the image positions.

The fitting procedure is performed in the same way as for the B1422+231 data. Again, image B is taken as a reference and the χ^2 -function is evaluated according to (4). We try to fit the positions and fluxes with SIE+SH and SIE+SH+NIS models. The flux ratios of the 11 sets of synthetic data, together with the results of the minimisation are presented in table 8. We experience similar problems fitting fluxes as before; the χ^2 -function value is high for all 11 data sets.

What might be surprising is the fact that we do not recover some properties of the lensing system. We know that the primary lens is fairly circular (one can *not* see that from fig. 2, since there, external shear is already added) and we know the values of the external shear components. What we also know *a priori* are the magnification factors for the images. These values were not recovered with high accuracy in model fitting.

For a smooth model and a source close to the cusp, the flux relation described before holds. We see that the fluxes violate this rule in all configurations we used. As we mentioned before this relation can only be violated when the source is away from the cusp or if there is substructure in the system. Since here we know the source position, the N-body lensing results show that the substructure we have in this particular simulated galaxy is indeed responsible for the observed deviation.

6.3. Discussion of the results from N-body lensing

An important question is whether the N-body simulation galaxy we are using is a good representation of a real galaxy for the purpose of lensing. If the resolution is not high enough, an N-body simulated galaxy might show more substructure than a real galaxy has.

In order to obtain the surface mass density map representative of lensing and to try to make sure that the substructure we see is not of numerical origin we used a

smoothing length for particles of $\sigma = 0.8 \text{ kpc} \sim 0.2 \text{ arcsec}$. The individual mass clumps we see in the corresponding surface mass density map (Fig. 1) therefore contain well above 100 particles. As we mentioned before, a realistic resolution scale for an identified substructure in the simulation corresponds to ~ 40 particles.

The regions that are interesting for multiple image formation typically have κ values of about 1. There we have approximately 300 particles per σ^2 which gives a Poisson noise of $1/\sqrt{N} \sim 1/\sqrt{300} \sim 0.06$. Therefore, any deviation of κ due to substructure larger than this value tells us that we are probably dealing with “physical” substructure, i.e. not of numerical origin. Our surface mass density maps show deviations well above the Poisson noise.

These two conclusions make us confident that the data, especially the substructure we are using for determining lensing properties, are of physical origin. We have seen that such a level of substructure can influence lensing phenomena a lot; In particular the synthetic fluxes we obtained deviate highly from those predicted by smooth models. In order to make stronger conclusions one would have to investigate many different realisations of N-body simulated galaxies to see whether they all show the same properties in terms of strong gravitational lensing.

7. Conclusion

In this work we have investigated the influence of substructure in the gravitationally lensed system B1422+231. While it is intuitively clear that a lens galaxy is not a smooth entity, we have tried to investigate how deviation from a smooth model can influence lensing phenomena, especially the image flux ratios.

We have used two different smooth models for the lensing galaxy (SIE+SH and NIE+SH), and both failed very badly in fitting the image fluxes (we got $\chi^2 = 130$ with 2

Table 8. The flux ratios of image A, C and D w.r.t. image B of 11 data sets with different image positions β_s (see also Fig. 4). Listed are also the resulting χ^2 values for fitting image positions and fluxes with SIE+SH model (χ_1^2) and SIE+SH+NIS model (χ_2^2). The core radius and σ_{NIS} of the perturbing galaxy were fixed to the values $\theta_c = 1 \text{ mas}$ and $\sigma_{\text{NIS}} = 15 \text{ km/s}$.

Data set	F_{AB}	F_{CB}	F_{DB}	χ_1^2	χ_2^2
1	1.04	0.80	0.220	120	2.0
2	1.29	1.20	0.193	960	120
3	1.43	1.40	0.167	2100	190
4	1.20	0.79	0.142	660	5.1
5	1.06	0.59	0.116	350	3.9
6	1.05	0.42	0.089	150	81
7	1.06	0.31	0.064	450	110
8	0.60	0.29	0.047	93	40
9	0.51	0.46	0.051	400	180
10	0.59	0.52	0.064	86	9.3
11	0.62	0.66	0.070	240	36

degrees of freedom). The use of models with substructure requires additional observational constraints. Therefore, we used deconvolved image shapes as constraints. We get a significant improvement of the fit compared to the smooth model. However, the way the substructure is introduced is oversimplified, thus we should not be surprised that the resulting χ^2 is still high. For the model with a single perturber we got $\chi^2 = 19$ for 6 degrees of freedom, and with two perturbers we had $\chi^2 = 15$ for 4, while the model without substructure (where deconvolved image shapes were included) gives $\chi^2 = 140$ for 8 degrees of freedom.

Up to now we have not considered the possibility that microlensing plays a role for the radio fluxes. Koopmans & de Bruyn (2000) claim that they have detected microlensing in the multiply-imaged radio source B1600+434. Microlensing is a very tempting explanation for difficulties in fitting the fluxes for it can also explain why the 8.4 GHz A:B flux ratio has changed from 0.97 in 1991 (Patnaik et al. 1992) to 0.93 in 1997 (Patnaik et al. 1999). This has a consequence that again speaks in favour of substructure, since the presence of radio microlensing indicates that there is a significant number of compact objects in the lens galaxy halo.

N-body simulation data of a model galaxy provides a test for the influence of mass-substructure in strong gravitational lensing. When we generated data of four image systems with the simulated galaxy we again experienced difficulties. We have tried to fit image positions and fluxes and failed to obtaining a model that fits well. From these experiments we can conclude that the level of substructure obtained from this particular N-body simulated galaxy can cause the same difficulties as experienced in some of the real gravitationally lensed systems.

In order to obtain stronger conclusions one would have to investigate more realisations of simulated galaxies, also at different redshifts. However, the fitting of B1422+231 and the N-body simulation results indicate that substructure plays an important role in strong lensing.

In particular, modelling B1422+231 and the synthetic data show that the fluxes of all images are affected by the substructure. One should therefore avoid using the flux constraints directly; they should, rather, be treated in statistical manner, e.g. in a way suggested by Mao & Schneider (1998). Fortunately, the perturbations on the scales we are dealing with here do not influence the image positions significantly, and play even less of a role for the time delay. Strong lensing thus remains one of the best tools to constrain the Hubble constant.

Acknowledgements. We would like to thank Douglas Clowe and Alok Patnaik for many useful discussions. This work was supported by the Bonn International Physics Programme, by the Deutsche Forschungsgemeinschaft, and by the TMR Network “Gravitational Lensing: New Constraints on Cosmology and the Distribution of Dark Matter” of the EC under contract No. ERBFMRX-CT97-0172.

References

Bartelmann, M. & Schneider, P. 2001, *Phys. Rep.*, 340, 291

Bradač, M. 2001, Substructure in the Gravitationally Lensed System B1422+231, Diploma Thesis, University of Bonn (Aug 2001)

Chang, K. & Refsdal, S. 1979, *Nature*, 282, 561

Chiba, M. 2001, *astro-ph/0109499*

Dalal, N. & Kochanek, C. 2001, *astro-ph/0111456*

Falco, E., Lehar, J., & Shapiro, I. 1997, *AJ*, 113, 540

Fassnacht, C., Blandford, R., Cohen, J., Matthews, K., Pearson, T., Readhead, A., Womble, D., Myers, S., Browne, I., Jackson, N., Marlow, D., Wilkinson, P., Koopmans, L., de Bruyn, A., Schilizzi, R., Bremer, M., & Miley, G. 1999, *AJ*, 117, 658

Hogg, D. & Blandford, R. 1994, *MNRAS*, 268, 889

Impey, C., Foltz, C., Petry, C., Browne, I., & Patnaik, A. 1996, *ApJ*, 462, L53

Keeton, C. & Kochanek, C. 1997, *ApJ*, 487, 42

—. 1998, *ApJ*, 495, 157

Keeton, C., Kochanek, C., & Seljak, U. 1997, *ApJ*, 482, 604

Kochanek, C., Falco, E., Impey, C., Lehár, J., McLeod, B., Rix, H., Keeton, C., Muñoz, J., & Peng, C. 2000, *ApJ*, 543, 131

Koopmans, L. & de Bruyn, A. 2000, *A&A*, 358, 793

Kormann, R., Schneider, P., & Bartelmann, M. 1994, *A&A*, 286, 357

Kundic, T., Hogg, D., Blandford, R., Cohen, J., Lubin, L., & Larkin, J. 1997, *AJ*, 114, 2276

Mao, S. & Schneider, P. 1998, *MNRAS*, 295, 587

Metcalf, R. & Madau, P. 2001, *astro-ph/0108224*

Metcalf, R. & Zhao, H. 2001, *astro-ph/0109499*

Navarro, J. & Steinmetz, M. 1997, *ApJ*, 478, 13

Patnaik, A., Browne, I., Walsh, D., Chaffee, F., & Foltz, C. 1992, *MNRAS*, 259, 1P

Patnaik, A., Kemball, A., Porcas, R., & Garrett, M. 1999, *MNRAS*, 307, L1

Press, W., Teukolsky, S., Vetterling, W., & Flannery, B. 1992, Numerical recipes in FORTRAN. The art of scientific computing (Cambridge: University Press, 2nd ed.)

Refsdal, S. 1964, *MNRAS*, 128, 307

Schneider, P., Ehlers, J., & Falco, E. 1992, Gravitational Lenses (Gravitational Lenses, Springer-Verlag Berlin Heidelberg New York.)

Schneider, P. & Weiss, A. 1992, *A&A*, 260, 1

Steinmetz, M. 1996, *MNRAS*, 278, 1005

Steinmetz, M. & Navarro, J. 2000, in ASP Conf. Ser. 197: Dynamics of Galaxies: from the Early Universe to the Present, 165

Steinmetz, M. & Navarro, J. 2001, *NewA* submitted